IAEA nuclear fusion

PAPER • OPEN ACCESS

Investigation of fast ion characteristics via neutron emission spectroscopy in NBI–ICRF third-harmonic heating plasmas on EAST

To cite this article: A.D. Xu *et al* 2026 *Nucl. Fusion* **66** 066024

OPEN ACCESS
IOP Publishing | International Atomic Energy Agency
Nuclear Fusion
Nucl. Fusion 66 (2026) 066024 (13pp) https://doi.org/10.1088/1741-4326/ae6929

Investigation of fast ion characteristics via neutron emission spectroscopy in NBI–ICRF third-harmonic heating plasmas on EAST

A.D. Xu[1,a], Y.H. Li[1,a], T. Yu[1], J.Y. Zhang[1], M.Y. Xu[2], C.Y. Pan[2], B.L. Hao[3], Y.Q. Zhang[2], Z.S. Liu[1], X.T. Xu[1], Z.Y. Wang[1], Y.B. Zhang[2], M. Nocente[4], G. Gorini[4,5], M. Tardocchi[5], X.Q. Li[1], J. Huang[2], L.Q. Hu[2], W. Zhang[2], X.J. Zhang[2], G.Q. Zhong[2], T.S. Fan[1,2,*], B.N. Wan[2,*] and The EAST Team[b]

[1] State Key Laboratory of Nuclear Physics and Technology, School of Physics, Peking University, Beijing, China
[2] Institute of Plasma Physics, Chinese Academy of Sciences, Hefei, China
[3] Southwestern Institute of Physics, Chengdu, China
[4] Department of Physics, University of Milano-Bicocca, Milan, Italy
[5] Institute for Plasma Science and Technology, National Research Council (CNR), Milan, Italy

E-mail: tsfan@pku.edu.cn and bnwan@ipp.ac.cn

Received 16 December 2025, revised 24 February 2026
Accepted for publication 6 May 2026
Published 27 May 2026

Abstract

We present the first comprehensive multi-sightline neutron spectrometry measurements during synergistic NBI and deuterium third-harmonic ICRF heating on EAST. Using the time-of-flight enhanced diagnostic (TOFED) and three compact organic scintillator spectrometers, we observed a significant broadening in the measured spectra, indicating the acceleration of fast ions well beyond the injection energy. TRANSP simulations reveal a fast ion distribution extending to approximately 600 keV with a marked pitch-angle asymmetry favoring co-current velocities. These simulations are validated by synthetic spectra generated via the GENESIS code and the spectrometers' instrumental response functions, which show excellent agreement with measurements. Furthermore, a TRANSP-independent weight-function analysis of the spectral cutoffs confirms the pitch asymmetry of the energetic tail. Orbit-topology calculations using the Orbit Weight Computational Framework (OWCF) demonstrate that this asymmetry is determined by the fast ion loss boundaries on EAST. These results establish the capability of multi-sightline neutron spectrometry to unveil the phase-space distribution of radiofrequency-accelerated ions, serving as a vital diagnostic for MeV-range fast ion physics relevant to future burning plasma research.

[a] The first two authors gave equal contributions to this work.
[b] See Gong *et al* 2024 (https://doi.org/10.1088/1741-4326/ad4270) for the EAST Team.
[*] Authors to whom any correspondence should be addressed.

Keywords: neutron emission spectroscopy, fast ions, ion cyclotron resonance heating, neutral beam injection, EAST tokamak

(Some figures may appear in colour only in the online journal)

1. Introduction

Magnetic confinement fusion research is approaching the burning plasma stage. In such deuterium–tritium (DT) burning plasmas, the 3.5 MeV α particles will dominate plasma heating. These MeV-range fast ions will undergo phase-space interactions with radiofrequency (RF) waves, instabilities, and turbulence, thereby strongly influencing plasma behavior [1]. Therefore, measuring the fast ion velocity distribution function offers a direct experimental basis for studying these crucial processes [2].

In deuterium plasmas, auxiliary heating such as neutral beam injection (NBI) and ion cyclotron range of frequencies (ICRF) heating are the primary sources of fast ions. The combination of NBI and nth harmonic ICRF heating ($n = 2, 3$, typically) provides an effective means to generate MeV-range fast deuterium ions, serving as experimental surrogates for fusion-born α particles in deuterium plasmas. The NBI supplies energetic seed ions, which can be further efficiently accelerated by the ICRF waves due to finite Larmor radius effects [3, 4]. Synergistic heating combined with NBI and third-harmonic ICRF for deuterium ($\omega \approx 3\omega_{\mathrm{cD}}$), rather than the second-harmonic ICRF ($\omega \approx 2\omega_{\mathrm{cD}}$), avoids fundamental absorption by hydrogen ions and more effectively produces high-energy deuterons. This heating scenario has been demonstrated on devices including TEXTOR [5], JET [6, 7], ASDEX-U [8], and EAST [9].

Neutron spectroscopy provides diagnostics of the kinetic information of fuel ions through the measurement of fusion neutron energy spectra [10, 11]. In deuterium plasmas, neutron emission is dominated by beam–thermal reactions between fast and thermal ions, so the neutron energy spectra contain valuable information on the fast ion velocity distributions [12, 13]. On JET deuterium discharges, the neutron time-of-flight (tof) spectrometer TOFOR was used to measure the perpendicular (relative to the magnetic field) fast ion velocity distribution during NBI–ICRF synergistic heating [14] and to investigate interactions between fast ions and core-localized toroidal Alfvén eigenmodes (tornado modes) [15, 16]. Furthermore, neutron and gamma-ray spectroscopic measurements along multiple lines-of-sight (LOSs) have been shown to provide access to the parallel velocity (also relative to the magnetic field) of fast ions [17], enabling tomographic reconstructions of the MeV fast ion distribution $f(v_{\parallel}, v_{\perp})$ under NBI–ICRF third-harmonic heating [18, 19] and D–$\mathrm{D_{NBI}}$–^{3}He 3-ion ICRF heating scenarios [19–21]. Extending these studies to deuterium-tritium plasmas, JET D–T campaign demonstrated that, using a high signal-to-noise ratio magnetic proton recoil (MPR) spectrometer, MeV-range fast fuel ions produced by NBI–ICRF synergistic heating could be successfully diagnosed [22, 23], and the fast ion distribution of deuterium has been tomographically reconstructed in a tritium-rich plasma [24]. For future burning-plasma devices such as ITER, the high-resolution neutron spectrometer (HRNS), primarily designed for core D/T ratio measurements, is also expected to provide valuable information on fuel ion temperatures and fast ion velocity distributions [25].

On EAST, benefiting from improved ICRF antenna coupling efficiency [26], a series of NBI–ICRF synergistic heating studies have been performed. [9, 27–29] reported synergistic heating experiments combined with NBI and second or third harmonic ICRF waves, and the fast ion distributions were simulated. In addition, previous studies have calculated fast ion losses and heat fluxes under synergistic heating on EAST [30, 31]. Multiple neutron spectrometers have been developed on EAST [32], providing a capability to observe the synergistic effect. However, on EAST, quantitative analysis of neutron spectroscopy measurements under NBI–ICRF synergistic heating has not been reported previously.

This paper presents, for the first time, comprehensive multi-LOS neutron spectrometer measurements on EAST under NBI–ICRF third-harmonic heating. Pronounced spectral broadening was observed by all four neutron spectrometers. The fast ion velocity distribution function was calculated using the TRANSP code [33], and synthetic spectra were calculated by combining the GENESIS code [34] with the spectrometer response matrices. A weight-function analysis was applied to efficiently estimate the energy-pitch characteristics of the fast-ion tail. Both TRANSP simulations and weight-function analysis showed a pitch-angle asymmetry of the fast ion tail. Orbit analysis indicates that this asymmetry is caused by fast ion loss orbits on EAST. These results establish the basis for tomographic inversion of fast ion velocity distributions and provide diagnostic capability of MeV-range fast ions for burning plasma studies.

The remainder of this paper is organized as follows. Section 2 introduces the principle of diagnosing fast ion velocity distributions with neutron spectroscopy. Section 3 describes the EAST synergistic NBI–ICRF third-harmonic heating discharge and the multi-LOS neutron spectrometers system. Section 4 presents the measurement results, and section 5 analyzes the fast ion distribution using TRANSP simulations and spectrometer weight functions. Section 6 discusses the influence of orbit effects. Finally, conclusions are drawn in section 7.

2. Diagnostic principles and analysis methods

2.1. Influence of fast ions on neutron emission

In magnetic confinement fusion devices, the presence of energetic deuterium and tritium ions can substantially increase the

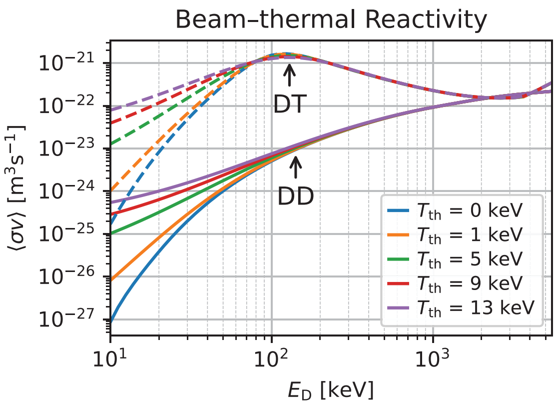

Figure 1. Beam–thermal fusion reactivities for monoenergetic deuteron beams interacting with Maxwellian deuterium or tritium ions. Solid lines denote DD reactions and dashed lines denote DT reactions. Different colors correspond to different ion temperatures.

neutron yield, as well as modify the neutron energy spectrum. For two-body fusion reactions $A+B\to n+C$ (where AB denotes either DD or DT reactions), the fusion neutron emission rate is given by

$$R_{AB}=\frac{n_A n_B}{1+\delta_{AB}}\langle\sigma v\rangle_{AB}, \tag{1}$$

where n_A and n_B denote the number densities of the ion species, and δ_{AB} is the Kronecker delta, taking the value 1 for identical species and 0 otherwise. The reactivity $\langle\sigma v\rangle$ can be expressed as

$$\langle\sigma v\rangle_{AB}=\iint \hat{f}_A(\boldsymbol{v}_A)\hat{f}_B(\boldsymbol{v}_B)\sigma_{AB}(v_{rel})v_{rel}\,d^3\boldsymbol{v}_A d^3\boldsymbol{v}_B, \tag{2}$$

where $v_{rel}=|\boldsymbol{v}_A-\boldsymbol{v}_B|$ is the relative velocity, $\sigma_{AB}(v_{rel})$ is the fusion cross section, and $\hat{f}_A(\boldsymbol{v}_A)$ and $\hat{f}_B(\boldsymbol{v}_B)$ are the normalized velocity distribution functions of species A and B, respectively. In deuterium plasmas of currently operating tokamaks with NBI injection, neutron emission is dominated by beam–thermal reactions between fast and thermal ions. Similarly, in present DT experiments with NBI, the majority of neutron emission also arises from beam–thermal reactions [35]. Figure 1 shows the beam–thermal fusion reactivity as a function of deuteron beam energy. The DD and DT reactions are indicated by solid and dashed lines, respectively, and the reaction cross sections are taken from the TENDL-2019 library [36].

For the case of NBI–ICRF synergistic heating, ICRF can further accelerate fast deuterons from ∼100 keV to the MeV range. As shown in figure 1, the DD reactivity (solid lines) increases markedly with beam energy within this range, whereas the DT reactivity (dashed lines) exhibits only a moderate increase (and can even decrease). This indicates that in deuterium plasma, the high-energy ICRF fast ion tail corresponds to an enhanced neutron emission, providing an opportunity to investigate the fast ion velocity distribution via neutron spectroscopy and yield measurements.

The influence of fast ions on the neutron emission spectrum is discussed below. For reactions $A+B\to n+C$, using classical kinematics, the emitted neutron energy E_{n0} in the laboratory frame can be written as [37]:

$$E_{n0}=\frac{1}{2}m_n v_{com}^2+\frac{m_c}{m_n+m_c}(Q+K)+m_n v_{com}\sqrt{\frac{2m_c(Q+K)}{m_n(m_n+m_c)}}\cos\theta_n', \tag{3}$$

where m_n and m_c represent the masses of the neutron and the other product particle, respectively; v_{com} is the center-of-mass velocity; Q and K are the reaction Q-value and the total kinetic energy of the reactants in the center-of-mass frame; and θ_n' is the neutron emission angle in that frame. The corresponding neutron emission spectrum, representing the number of neutrons emitted per unit volume (dV), per unit solid angle ($d\Omega_{lab}$), and per unit time (dt), is then given by [37]:

$$\frac{dN}{dV d\Omega_{lab}\,dt\,dE_n}=\frac{n_A n_B}{1+\delta_{AB}}\iint\delta(E_n-E_{n0})\hat{f}_A(\boldsymbol{v}_A)\hat{f}_B(\boldsymbol{v}_B)\times v_{rel}\sigma(v_{rel},\theta_n')\,d^3\boldsymbol{v}_A d^3\boldsymbol{v}_B. \tag{4}$$

Here, n_A and n_B denote the number densities of the reactants; $\hat{f}_A$ and $\hat{f}_B$ represent the normalized velocity distribution functions; $\boldsymbol{v}_{rel}=\boldsymbol{v}_A-\boldsymbol{v}_B$ is the relative velocity; and $\sigma(v_{rel},\theta_n')$ is the differential cross-section of the reaction. The Kronecker delta δ_{AB} is unity for reactions within the same particle population and zero otherwise. The terms E_{n0} and θ_n' are determined by equation (3) and the geometric relations of the velocities, which are expressed as functions of $\boldsymbol{v}_A$, $\boldsymbol{v}_B$, and the LOS angle β of the spectrometer.

Fast ions undergo both gyro motion and parallel motion in the background magnetic field. The former causes a broadening of the neutron emission spectrum, while the latter leads to a spectral shift. Simplified analytical treatments of these effects have been presented in [38]. Overall, the neutron emission spectrum carries information on the fast ion velocity distribution, but it also depends on the observation direction of the spectrometer LOS.

2.2. Weight functions of neutron emission spectroscopy

Under certain assumptions—namely, that the neutron emission arises mainly from the plasma core and is dominated by beam–thermal reactions—the neutron emission spectrum can be approximated by a linear function of the fast ion velocity distribution. In this case, a *weight function* can be defined to describe such linear mapping. More generally, weight functions are widely used in the analysis of various fast ion diagnostics [39], such as fast ion D_α (FIDA) [40–43], collective Thomson scattering (CTS) [44], neutral particle analyzers (NPAs) [45], fast-ion loss detector (FILD) [46, 47], ion cyclotron emission (ICE) [48, 49], 3 MeV proton diagnostics [50] as well as neutron emission spectroscopy (NES) [51–53] and gamma-ray spectroscopy (GRS) [54, 55]. The weight function $w(X,E,p)$ represents the contribution from an ion that has a

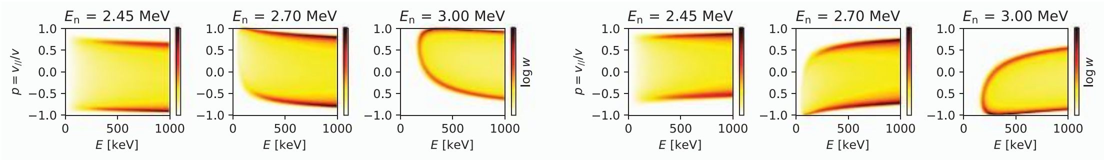

(a) $\beta = 54°$ (b) $\beta = 132°$

Figure 2. Weight functions of the DD neutron emission spectrum $w(E_n, E, p)$ for different LOS angles β.

specific energy-pitch (E, p) in velocity space to the diagnostic spectrum at X (where X represents a measurement bin of a given spectral width) and is formally defined as

$$w(X, E_0, p_0) = s(X)\bigg|_{f(E,p)=\delta(E-E_0)\delta(p-p_0)}, \tag{5}$$

where $f(E,p)$ is the fast ion velocity distribution, and $s(X)$ is the measured diagnostic spectrum. Using this definition, the diagnostic spectrum can be expressed as

$$s(X) = \int_E \int_p w(X, E, p) f(E, p)\, \mathrm{d}E\, \mathrm{d}p \tag{6}$$

and provides a means for rapid computation of synthetic diagnostic data or for tomographic inversion using appropriate algorithms [39]. On EAST, weight functions have been established for FIDA [43] and NES [52, 53] in the energy range $E < 100$ keV.

For a neutron spectrometer, the neutron spectral weight function $w(E_n, E, p)$ along the LOS is first calculated, and by convolving it with the detector's response matrix $r(X, E_n)$, the overall spectrometer weight function $w(X, E, p)$ can be obtained. As an example, we consider two LOSs of the EAST neutron spectrometer. Their neutron spectral weight functions were calculated using the GENESIS code [34], and the results are shown in figure 2. The LOS angles β, representing the angle between the plasma current and the detectors' line of sight, are 54° and 132°, respectively. These angles correspond to the EJ-301 and time-of-flight enhanced diagnostic (TOFED) detectors on EAST (illustrated in figure 4). It should be noted that, in this study, the sign convention of the pitch follows that used in TRANSP, where the pitch is defined as positive when parallel to the plasma current. The low-energy part of the neutron spectrum is affected by scattered neutrons, so the analysis mainly focuses on neutrons of $E_n > 2.45$ MeV. It can be seen through figures 2(*a*) and (*b*) that, the pitch-angle dependence of weight function arises from the LOS direction. Consequently, measurements from a single LOS leave certain regions of the (E, p) space uncovered, making it difficult to fully reconstruct the fast ion velocity distribution. Therefore, combining multiple LOS enables a more comprehensive coverage of the fast ion velocity space, which is beneficial for the analysis of NBI–ICRF synergistic heating scenarios.

It should be noted that, unlike FIDA, CTS, or active NPA diagnostics with high spatial resolution, the measured neutron spectrum integrates over the entire LOS. Järleblad *et al* extended the weight function of NES to fast ion orbit space (E, μ_m, R_m) [56] and successfully applied it to the fast-ion orbit analysis of the JET DTE2 campaign [24, 57]. However, as the neutron emission profile is strongly peaked, the approximation that neutrons are emitted primarily from the plasma core can be used. This approximation justifies the application of equation (6), as adopted in [18, 19, 21, 24, 51–53]. A detailed discussion of the neutron spectrometers' weight functions on EAST, as well as their application to NBI–ICRF heating experiments, is provided in section 5.2.

3. Experimental setup

3.1. The EAST discharge

A series of nine NBI–ICRF third-harmonic synergistic heating experiments were carried out on EAST between discharge shots #113828 and #113848. Shot #113829 was selected as a representative case for analysis. The evolution of shot #113829 is shown in figure 3(*a*). The basic parameters of the discharge were: line-averaged electron density $n_e = 2.8 \times 10^{13}$ cm^{-3}, plasma current $I_p = 0.50$ MA, core toroidal magnetic field $B_0 = 1.65$ T (counter-I_p direction). A drawing of the NBI trajectories and ICRF antenna locations are shown in figure 4. Two NBI lines, NBI1L and NBI2L, both in the co-current direction, were sequentially applied with beam voltages of 55 kV and 50 kV, and injection powers of 0.8 MW and 0.7 MW. Both the I and N port ICRF antennas delivered heating powers of 0.4 MW each, with a frequency of 37 MHz. Additionally, a 1.2 MW low hybrid wave power was injected for electron heating and current drive, and a $n = 2$ resonant magnetic perturbation was applied for impurity exhaust.

Two typical time points were selected: $t = 3.5$ s (NBI at full power, ICRF off) and $t = 4.5$ s (both NBI and ICRF on). At these times, electron density profiles from the reflectometer for the edge and the polarization-interferometer (POINT) for the core, electron temperature T_e from Thomson scattering, ion temperature T_i from x-ray crystal spectroscopy, and effective charge Z_{eff} from visible Bremsstrahlung were input into the ONETWO code [58] for equilibrium reconstruction. The resulting profiles are shown in figure 3(*a*). As illustrated in figure 3(*c*), the third-harmonic resonance layer for deuterium passed through the magnetic axis ($R_{axis} = 1.87$ m), whereas the second-harmonic layer for deuterium (also the fundamental resonance layer for minority hydrogen) was entirely outside the plasma.

Following the ICRF injection, the core electron density increased, while the electron and ion temperatures

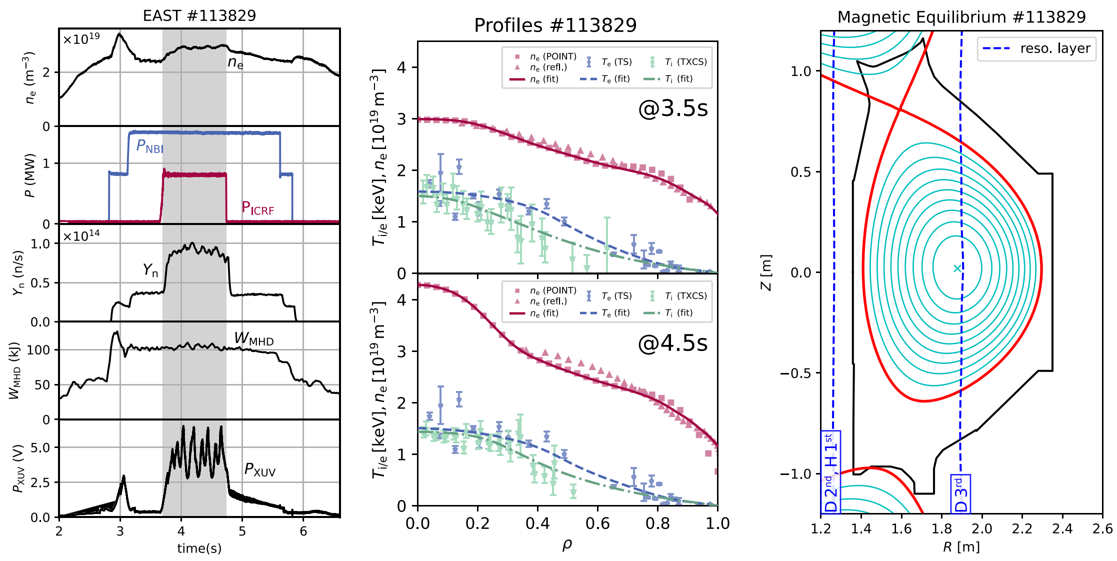

(a) Evolution (b) Profiles (c) Magnetic equilibrium

Figure 3. EAST discharge #113829: (*a*) time evolution of discharge parameters; (*b*) profiles measured before (3.5 s) and during (4.5 s) ICRF injection, where the radial coordinate ρ denotes the square root of the normalized toroidal flux $\sqrt{\phi_n}$; (*c*) magnetic equilibrium and resonance layer positions.

decreased slightly. The stored energy remained nearly constant at approximately 110 kJ, possibly due to impurity bursts triggered by ICRF, which temporarily reduced plasma confinement. As shown by the extreme ultraviolet intensity in figure 3(*a*), P_{XUV} increased noticeably after ICRF activation, indicating enhanced radiated power. Despite the negligible change in stored energy, after the application of ICRF power, the neutron yield Y_n more than doubled, rising from $3.7\times10^{13}\,\mathrm{N\,s^{-1}}$ to $9.1\times10^{13}\,\mathrm{N\,s^{-1}}$.

3.2. Neutron spectrometers

Neutron spectrometers on EAST are mainly installed at the F, H, and J ports, with three lines of sight in total, as illustrated in figure 4. The TOFED measures the neutron emission spectrum by recording the tof of neutrons that scatter once on the primary detector (S1) before reaching the secondary detector (S2). For a spherical flight path of radius R, the neutron flight time t_{tof} relates to neutron energy E_n as [10]:

$$t_{\mathrm{tof}} = \frac{2R}{\sqrt{2E_n/m_n}}. \quad (7)$$

The S2 detector of TOFED adopts a dual-ring configuration, which minimizes geometric and scintillator light transmission timing deviations, thereby optimizing energy resolution and detection efficiency [59]. With a flight path radius of 0.75 m, a typical 2.45 MeV D–D fusion neutron corresponds to a tof of 69 ns. The spectrometer is equipped with a digital data acquisition system, allowing background subtraction using the Double Kinematic Selection algorithm [60] to reduce the random coincidence background. TOFED is located outside the horizontal J port, approximately 13 m from the plasma, with its LOS angle $\beta = 132^\circ$ (for $R_{axis} = 1.87$ m). A 1.5 m-thick concrete wall provides shielding, and the diameter of the collimation hole is 4 cm. A compact stilbene crystal neutron spectrometer is also installed along the same LOS [61, 62]. TOFED results under NBI heating have been previously reported [63].

Additional compact neutron spectrometers were installed inside radiation shields located in the EAST hall. Since 2021, two newly designed radiation shields [64] have been installed in the EAST hall, facing the F and H ports, respectively [64]. The shield at the F port, with a LOS angle $\beta = 54^\circ$, houses an EJ-301 [37, 65] spectrometer, while the shield at the H port, with $\beta = 155^\circ$, contains a BC-501A spectrometer [66]. Stilbene, EJ-301, and BC-501A are all hydrogen-rich organic scintillators. Fast neutrons scatter off hydrogen nuclei, producing recoil protons that generate scintillation pulses, while pulse shape discrimination separates neutrons from gamma photons.

Among the four neutron spectrometers, the response functions for three of them—TOFED [52], EJ-301 [53], and stilbene [53]—have been established. Figure 5 illustrates the response spectra of these spectrometers for several monoenergetic neutron incidences. As shown in figure 5(*a*), the TOFED spectrometer exhibits a quasi-Gaussian response, where the peak position in the tof spectrum is uniquely determined by the neutron energy according to equation (7). In contrast, the EJ-301 and stilbene scintillators (figures 5(*b*) and (*c*)) show a quasi-rectangular response, where the pulse-height spectra are smoothly and broadly distributed up to a specific cutoff light-output energy. This continuous feature mainly arises from the kinematics of neutron-proton elastic scattering, where the energy deposited by the recoil proton is given by $E_p = E_n\cos^2\theta$. Since the scattering angle θ is stochastically distributed, it results in a broad energy range being covered.

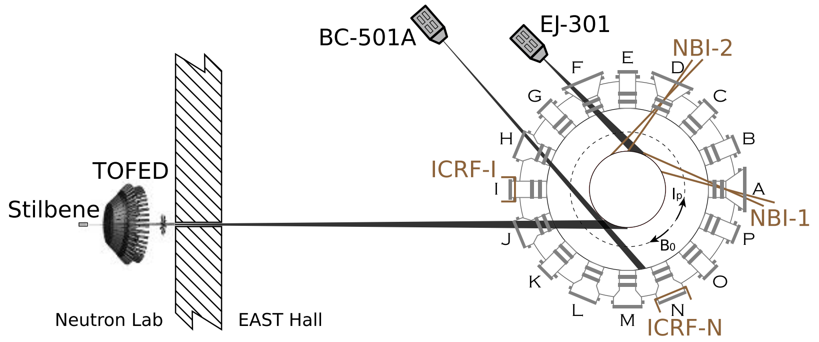

Figure 4. Schematic layout of neutron spectrometers and auxiliary heating systems on EAST.

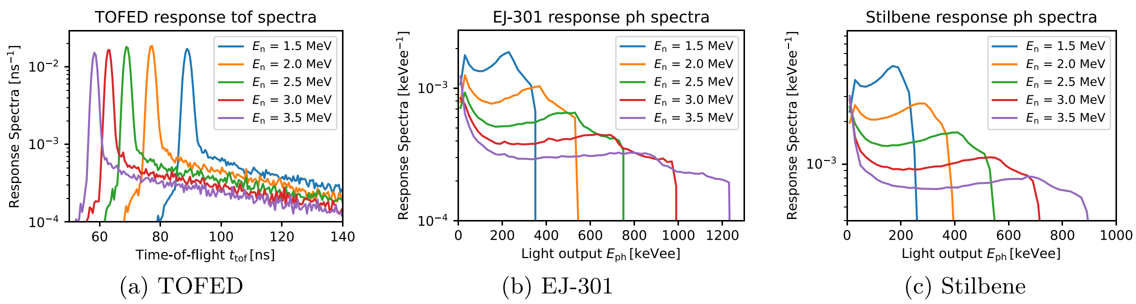

Figure 5. Response functions of the three neutron spectrometers for several monoenergetic neutron incidences ($E_n = 1.5,\ 2.0,\ 2.5,\ 3.0, 3.5$ MeV).

4. Results of neutron spectrometers

Using the four neutron spectrometers, pulse height (ph) or tof spectra of discharge #113829 were measured. The measurements were integrated over two time intervals corresponding to different heating conditions: full-power NBI without ICRF ($2.79-3.70$ s and $4.94-5.75$ s) and NBI–ICRF synergistic heating ($3.70-4.74$ s). The resulting spectra are shown in figure 6.

As shown in figure 6(*a*), synergistic heating produces a clear broadening of the TOFED tof spectra at both low and high tofs, indicating the generation of neutrons with higher and lower energies. In contrast, figures 6(*b*)–(*d*) show broadening only at the high-energy region, corresponding to higher-energy neutrons. This difference arises from the detectors' response functions, as discussed in section 3.2. For scintillator spectrometers, due to their quasi-rectangular response, the pulse-height spectra of lower-energy neutrons are buried under the high counts generated by the primary direct and scattered neutrons at the corresponding light-output energies.

5. Analysis of fast ion distribution functions

5.1. Forward modeling

The fast ion distribution functions under NBI and NBI–ICRF synergistic heating were simulated by the TRANSP [33] code, using the module NUBEAM [67] coupled with the ICRF solver TORIC [68]. The synergistic effects are incorporated in the NUBEAM RF-kick operator [69, 70], which treats the quasilinear diffusion term as a sudden change in the fast ion's velocity when traversing the resonance layer [71].

For EAST discharge #113829, the simulated fast ion distribution functions under NBI and NBI–ICRF synergistic heating are shown in figure 7. Figure 7(*a*) shows the volume- and pitch-angle-averaged $f(E)$, showing that ICRF further accelerates the NBI-injected beam ions, producing a high-energy tail extending up to about 600 keV. Figure 7(*b*) shows the 2D energy–pitch distribution under synergistic heating. The high-energy tail under synergistic heating is mainly located at positive pitches, primarily within the range $0 < p < 0.4$, which contrasts with the nearly pitch-symmetric tails (with respect to $p = 0$) observed in JET's NBI–ICRF third-harmonic synergistic heating discharges [4, 18]. This asymmetry is attributed to fast ion orbit effects, and will be analyzed in section 6.

The nuclear reaction kinetics code GENESIS [34] was used to calculate the different components of LOS-integrated neutron emission spectra (thermal–thermal, beam–thermal, and beam–beam). The code uses the plasma profiles, TRANSP-simulated fast ion distributions, and the spectrometer's LOS as inputs. The computed neutron spectra were subsequently convolved with the previously obtained scattering matrices [72] and the detectors' response functions [52, 53] to generate the synthetic diagnostic data. Forward modeling was then performed to separately scale the direct and scattered contributions using free coefficients a_{direct} and $a_{scatter}$. These synthetic

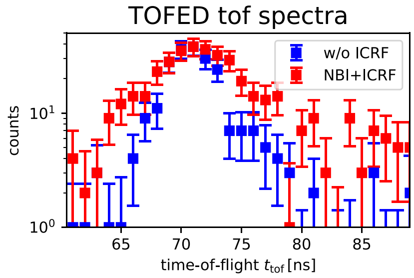

(a) TOFED time-of-flight spectra

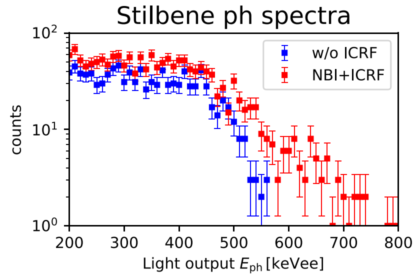

(b) Stilbene pulse height spectra

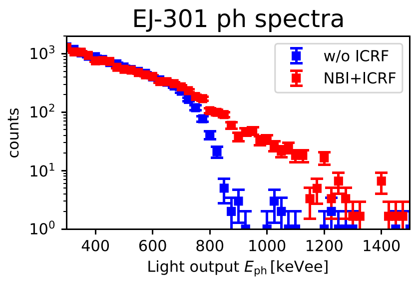

(c) EJ-301 pulse height spectra

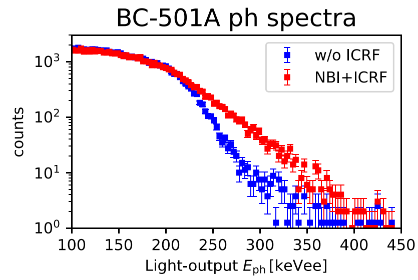

(d) BC-501A pulse height spectra

Figure 6. Comparison of neutron spectrometer measurements for EAST discharge #113829 under full-power NBI and NBI–ICRF synergistic heating. Error bars represent 1σ statistical uncertainties ($\sqrt{N}$, where N is the raw counts per bin; for TOFED, before background reduction).

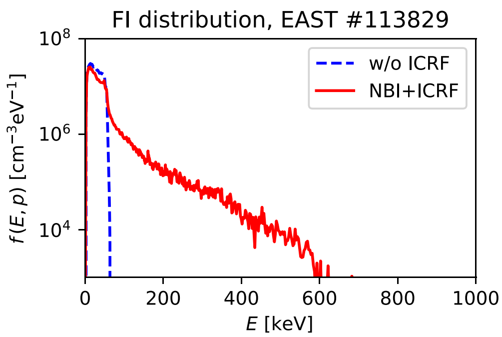

(a) Volume- and pitch-angle-averaged $f(E)$.

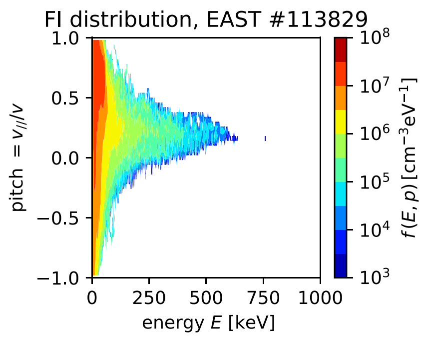

(b) Volume-averaged $f(E,p)$.

Figure 7. Fast ion velocity distribution functions calculated by the TRANSP code for EAST discharge #113829, averaged over the core region (normalized poloidal flux $\psi_n < 0.3$).

spectra were compared with the experimental data using the Cash statistic [73] as a goodness of fit:

$$C = 2\sum_{i=1}^{N}\left(s_i - e_i + e_i \ln\frac{e_i}{s_i}\right), \tag{8}$$

where N is the number of spectral bins, and s_i and e_i are the simulated and experimental counts in bin i, respectively. The Cash statistic is particularly suitable for low-count, Poisson-distributed neutron spectroscopic data.

As shown in figure 8, the forward modeling was applied to the TOFED, EJ-301, and stilbene data. The BC-501A spectrometer was excluded from the fitting analysis as the corresponding response matrix has not yet been established. The fitting results show good agreement with the experimental data under NBI heating (figures 8(*a*)–(*c*)). Besides, during NBI–ICRF synergistic heating, the spectral broadening observed in TOFED and stilbene (figures 8(*d*) and (*e*)) is well reproduced by simulations. For the EJ-301 spectrometer (figure 8(*f*)), agreement is good below 900 keVee. However, above 900 keVee, the experimental tail decreases more slowly than the simulated beam–thermal spectrum. This discrepancy is possibly due to pile-up events at high count rates, which have also been reported on JET [74]. By applying a forward pile-up simulation (similar to [74]), the agreement can be significantly improved, as shown in figure 8(*f*). In figure 8, the 'cutoff' positions—defined as the point where the dominant beam–thermal component drops to 1 count—are indicated by vertical cyan dashed lines. In the absence of ICRF (top panels (*a*)–(*c*)), the cutoffs for TOFED, stilbene, and EJ-301 are 65 ns, 570 keVee, and 870 keVee, respectively. Under NBI–ICRF synergistic heating (bottom panels *d*–*f*), the synergistic effect leads to significant spectral broadening,

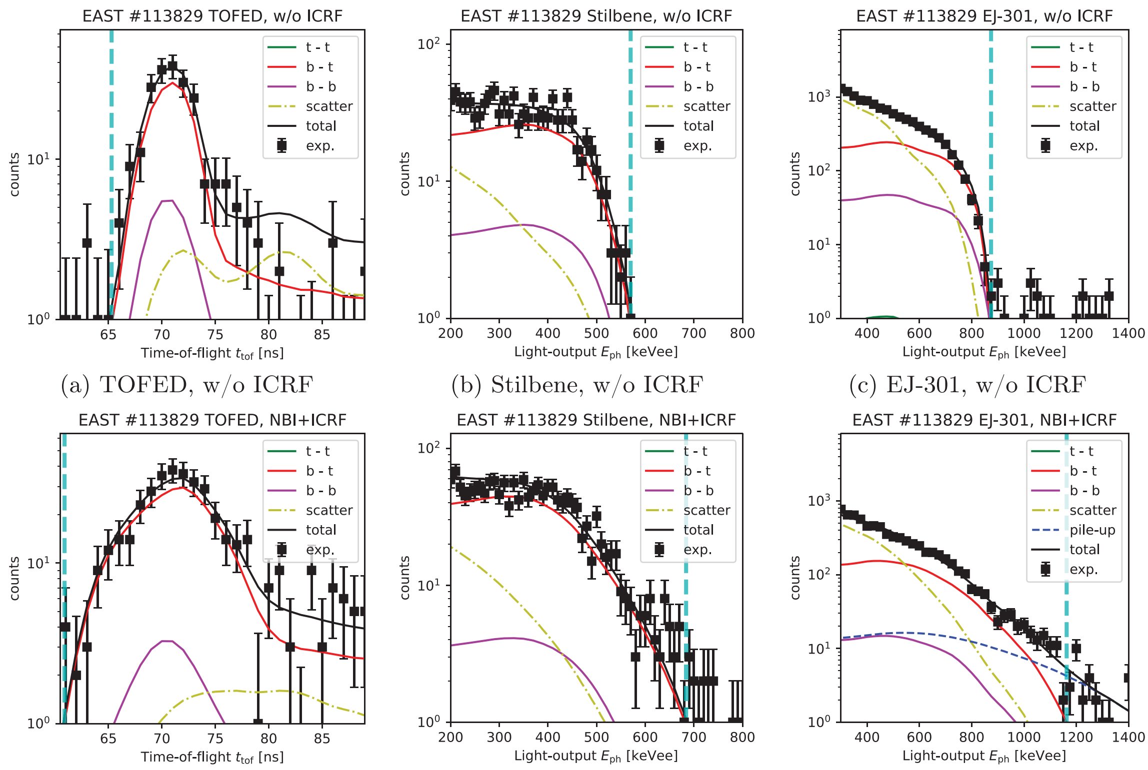

(a) TOFED, w/o ICRF (b) Stilbene, w/o ICRF (c) EJ-301, w/o ICRF

(d) TOFED, with ICRF (e) Stilbene, with ICRF (f) EJ-301, with ICRF

Figure 8. Comparison of measured and forward-modeled spectra for EAST discharge #113829 under full-power NBI and NBI–ICRF synergistic heating. The different spectral components are shown: thermonuclear (green solid line), beam–thermal (red solid line), beam–beam (magenta solid line), and scattered neutrons (yellow dash-dotted line). The total modeled spectrum is represented by the black solid line. Vertical cyan dashed lines indicate the detector cutoffs. Experimental data (black squares) are shown with error bars representing 1σ statistical uncertainties ($\sqrt{N}$).

with the cutoffs shifting to 61 ns, 680 keVee, and 1160 keVee, respectively.

5.2. Weight function analysis

Weight functions provide a direct and efficient way to extract fast ion velocity distributions from experimental data, without relying on TRANSP-based modeling or time consuming Monte Carlo simulations. Following previous works [52, 53], weight functions for TOFED and EJ-301 were recalculated for their upgraded LOS by the GENESIS code, extending the fast ion energy range to 1 MeV. The ion temperature was set to 1.5 keV. The neutron emission spectrum weight functions $w(E_n, E, p)$ calculated in section 2.2 were convolved with the spectrometers' response functions to obtain the spectrometer weight functions $w(X, E, p)$, with the results shown in figure 9.

Figures 9(*a*)–(*e*) show the TOFED weight functions at five selected tofs, and figures 9(*f*)–(*j*) display those of EJ-301 at five electron-equivalent light-output energies. Compared with $E < 100$ keV, all weight functions exhibit much higher sensitivity in the $E > 100$ keV range, which corresponds to the typical energies of fast ions under NBI–ICRF synergistic heating. This further confirms the diagnostic advantage of neutron spectrometers in such heating scenarios. The pitch-angle dependence of the weight functions mainly arises from the LOS, as discussed in section 2.1. Apart from the LOS effect, TOFED and EJ-301 weight functions also show distinct features: the TOFED weight functions exhibit peaks near the boundaries, whereas those of EJ-301 have a much coarser sensitivity to the fast ion velocity space. This difference arises from their response characteristics—TOFED has a quasi-Gaussian response to monoenergetic neutrons, whereas EJ-301 has a quasi-rectangular one.

Once weight functions are established, fast ion distribution functions can be obtained via tomographic inversion technique. However, on EAST, high-energy tails (figure 7(*b*)) do not satisfy $v_\perp \gg v_\parallel$, preventing 1D reduction [14, 15]. Full 2D inversion also requires complex numerical treatment [45]. To address these challenges, inspired by the 'null-measurement' method used in FIDA tomographic inversion [75], a fast method was adopted to determine the 'tip' of the fast-ion tail in (E, p) space based on spectral cutoffs. Here, the 'tip' is defined as the maximum energy–pitch extent reached by the fast-ion distribution. According to the principle of the null-measurement method, for any measurement bin X located within the null-measurement region—where the counts drop to the background level or become statistically negligible—the fast-ion distribution function $f(E, p)$ must be zero in the phase space region where the corresponding weight function $w(X, E, p)$ is non-zero.

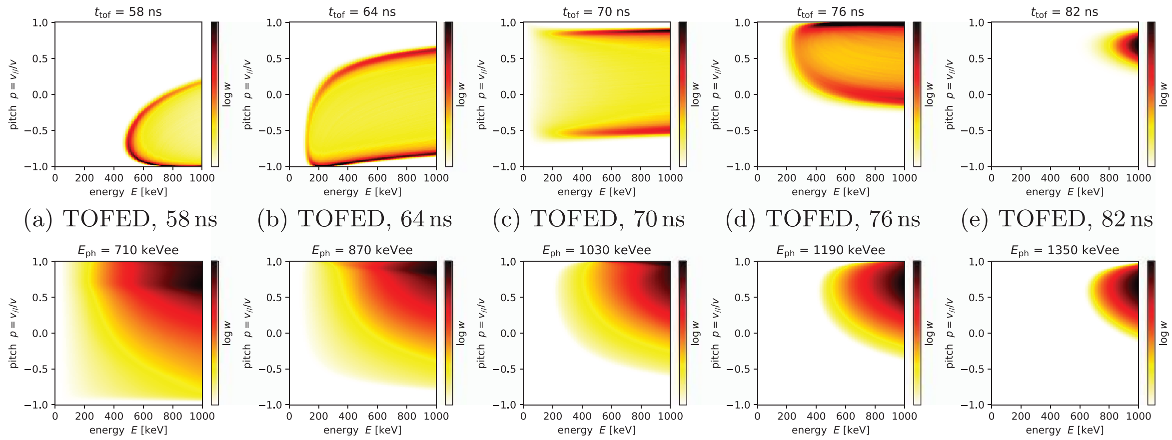

(a) TOFED, 58 ns (b) TOFED, 64 ns (c) TOFED, 70 ns (d) TOFED, 76 ns (e) TOFED, 82 ns

(f) EJ-301, 710 keV (g) EJ-301, 870 keV (h) EJ-301, 1030 keV (i) EJ-301, 1190 keV (j) EJ-301, 1350 keV

Figure 9. Weight functions for TOFED and EJ-301 neutron spectrometers. All data are normalized and logarithmically scaled.

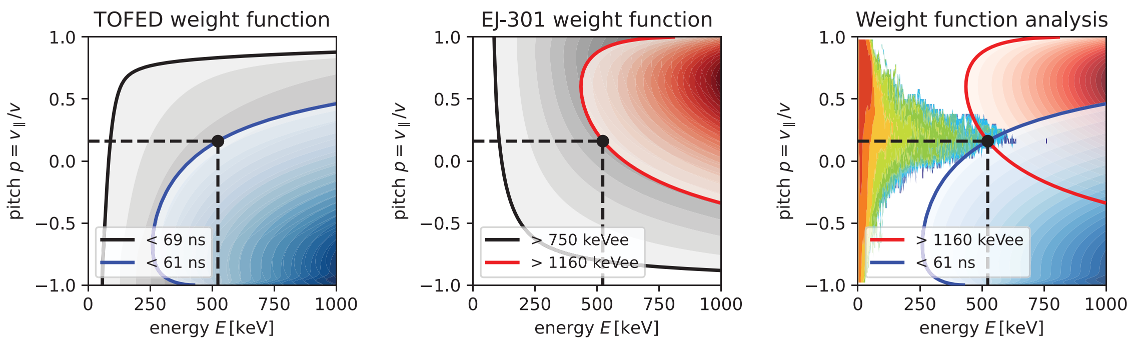

(a) TOFED (b) EJ-301 (c) Weight function analysis

Figure 10. Weight function analysis for determining the tip of the fast-ion tail in (E,p) space. In (*a*) and (*b*), blue and red contours represent the 'null-spaces' for TOFED and EJ-301, respectively, with their boundaries highlighted by thick solid lines of the same color. Gray contours indicate the phase space coverage for high-energy regions where the influence of scattered neutrons is relatively small, with their boundaries marked by black solid lines. (*c*) The intersection of the two null-space boundaries (marked by a black dot) identifies the tip of the fast-ion tail at $E \approx 520$ keV and $p \approx 0.2$. The background color map in (*c*) shows the fast-ion distribution function calculated by TRANSP (same as figure 7(*b*)), which is in good agreement with the tip determined from the intersection of the experimental spectral cutoffs.

For the TOFED and EJ-301 spectrometers, the spectral regions beyond the cutoffs ($t_{\rm tof} < 61$ ns and $E_{\rm ph} > 1160$ keVee, cyan lines in figures 8(*d*) and (*f*)) are identified as the null-measurement regions. We calculated the gross weight functions by summing the weight functions of all bins within these regions. The resulting 'null spaces' in (E,p) coordinates are shown as blue contours for TOFED in figure 10(*a*) and red contours for EJ-301 in figure 10(*b*), with their respective boundaries highlighted by thick blue and red solid lines. Additionally, the phase space coverage for the high-energy spectral regions of interest, where the influence of scattered neutrons is relatively small, is represented by gray contours and thick black solid lines in figures 10(*a*) and (*b*).

The tip of the fast-ion tail in velocity space is expected to be located at the intersection of the null-space boundaries from these two spectrometers with different lines-of-sight. As illustrated in figure 10(*c*), this intersection (marked by a black dot) corresponds to an energy of 520 keV and a pitch of 0.2. The distribution function calculated by TRANSP is also overlaid in figure 10(*c*), showing that the intersection point is in good agreement with the simulated distribution boundary. This consistency validates the weight function analysis and further confirms the asymmetric pitch distribution of fast ions under NBI–ICRF third-harmonic synergistic heating on EAST.

6. Fast ion orbit analysis

The distinct pitch-angle asymmetry of the fast ion velocity distribution, as consistently indicated by the TRANSP simulation and the weight function analysis, can be attributed to orbit loss effects on EAST. For the magnetic equilibrium of EAST #113829, the fast ion orbit topology was calculated using the Orbit Weight Computational Framework (OWCF) [76, 77]. OWCF constructs the fast ion orbit phase space as $(E, p_{\rm m}, R_{\rm m})$, where E is the fast ion energy, while $R_{\rm m}$ and $p_{\rm m}$ denote maximum major radius when crossing the midplane, and the associated pitch in this location. The orbit topology at $R_{\rm m} = 1.87$ m (magnetic axis) for different E and $p_{\rm m}$ is shown in

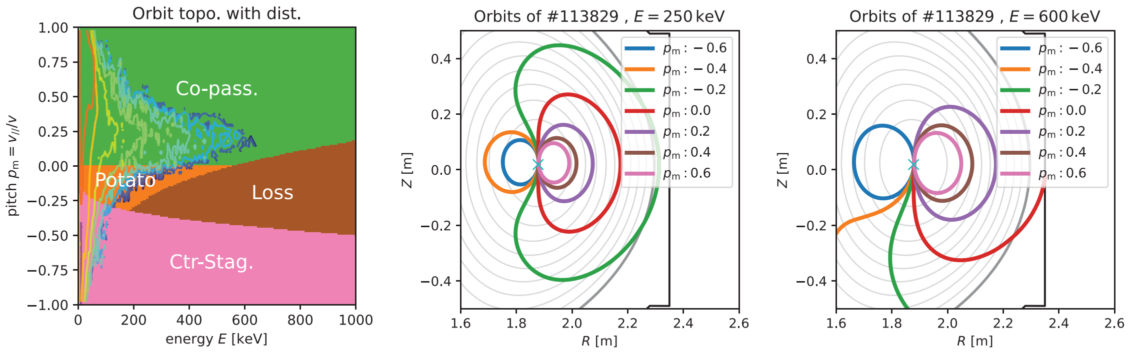

(a) Fast ion orbit topology (b) Fast ion orbits at 250 keV (c) Fast ion orbits at 600 keV

Figure 11. Core fast ion orbits at $R_m = 1.87$ m for #113829: (*a*) OWCF-calculated orbit topology with TRANSP velocity distribution overlaid; (*b*), (*c*) typical orbits with different initial pitch angles at 250 keV and 600 keV, respectively.

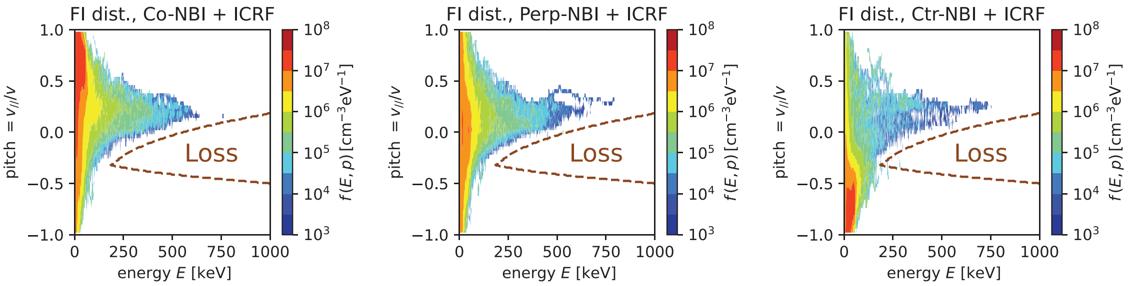

(a) Co-injection (same as figure 7b) (b) Perpendicular injection (c) Counter-injection

Figure 12. TRANSP-calculated fast ion velocity distributions under NBI–ICRF third-harmonic synergistic heating for (*a*) co-injection, (*b*) perpendicular-injection, and (*c*) counter-injection.

figure 11(*a*),[6] with the TRANSP-calculated core fast ion velocity distribution overlaid in the same figure. Typical orbits for energies of 250 keV and 600 keV, with different initial pitch angles are shown in figures 11(*b*) and (*c*).

The close alignment between the loss boundary and the fast ion tail in figure 11(*a*) suggests that orbit losses are responsible for the observed pitch asymmetry. Specifically, most lost orbits occur at negative pitches, and the range of pitches that lead to orbit loss widens as the fast ion energy increases. In the absence of orbit losses, the solution of Fokker–Planck equation under ICRF heating yields a nearly pitch-symmetric distribution. On EAST, however, orbit losses distort this distribution, ultimately producing a stable, asymmetric fast ion tail concentrated at positive pitches.

To rule out the possibility that the pitch-asymmetric distribution is due to the co-injected NBI, TRANSP simulations were performed with varied NBI injection directions while keeping the power fixed. The calculated fast ion distributions for co-, perpendicular-, and counter-injection NBI are shown in figures 12(*a*)–(*c*). The NBI injection direction mainly affects the pitch-angle distribution at lower-energy region ($E < E_{\mathrm{NBI}}$), whereas the high-energy fast ion tail consistently remains at positive pitches, aligned with the lost-orbit boundary. This further confirms that the observed pitch-asymmetry is governed by orbit-loss effects on EAST.

Orbit effects under ICRF heating also modify the spatial distribution of fast ions [78], potentially affecting the neutron emission profile. A complete analysis of these orbit effects using neutron camera data will be pursued in future work.

7. Conclusion

In this work, multi-LOS neutron spectrometers were used to measure fast ions under NBI–ICRF third-harmonic synergistic heating on EAST. All four neutron spectrometers show broadening of the spectrum under synergistic heating, indicating the production of higher-energy fast ions. Forward modeling and weight function analysis were applied to the fast ion distribution, showing good agreement and confirming the presence of a fast ion tail at approximately 600 keV with positive pitches in the experimental discharge.

These results demonstrate that multi-LOS neutron spectrometry can capture the two-dimensional fast ion velocity distribution in (E, p) space under synergistic heating. Future work will focus on tomographic inversion of high-energy fast ion velocity distribution using multi-LOS neutron spectrometry data. On EAST, multi-LOS FIDA measurements have already successfully reconstructed the low-energy fast ion distribution

[6] In the original OWCF code, orbits are labeled 'invalid' if a midplane crossing larger than R_m is found. We disabled this check for figure 11(*a*) to allow the magnetic axis to act as either the maximum or minimum crossing radius, ensuring all orbits originating from the axis are represented.

[42, 43, 79]. Combining these FIDA measurements with multi-LOS neutron spectrometry is expected to enable tomographic reconstruction of the fast ion distribution across the full energy range on EAST.

Furthermore, on EAST, orbit-loss effect causes a pronounced pitch-angle asymmetry in the fast ion distribution. The fast ion losses under synergistic NBI–ICRF heating can be further investigated using the FILDs on EAST [80, 81]. In addition, ICRF-induced orbit effects can also lead to spatial redistribution of fast ions, which can be studied by the radial neutron camera on EAST [82].

In next-step burning plasma devices such as ITER [83], BEST [84], SPARC [85], and CFETR [86], NBI and ICRF heating will serve as the main sources of auxiliary ion heating. In D–T operation, the neutron yield from RF-induced fast ion tails will be much weaker than those from thermal–thermal and NBI-beam–thermal reactions, making their diagnosis particularly challenging [87]. High-resolution, high signal-to-noise neutron spectrometers, such as magnetic proton recoil [88–90] or thin-foil proton recoil [91, 92] spectrometers should be proposed to provide comprehensive diagnostics of DT fuel-ions in this historic stage of fusion research.

Acknowledgments

This work was supported by the National MCF Energy R&D Program of China (Grant No. 2019YFE03040000). We gratefully acknowledge the staff members at EAST (https://cstr.cn/31130.02.EAST) for their technical support and assistance with data collection and analysis. We also thank Dr Henrik Järleblad at the Technical University of Denmark and his colleagues for making the Orbit Weight Computational Framework (OWCF) code publicly available, which provided essential tools for this study.

ORCID iDs

A.D. Xu 0000-0002-7967-8468
Y.H. Li 0009-0005-2894-0007
T. Yu 0009-0003-3734-6240
J.Y. Zhang 0009-0004-8863-8320
C.Y. Pan 0009-0003-2516-1441
B.L. Hao 0000-0003-3009-0660
Z.S. Liu 0009-0000-3285-9117
X.T. Xu 0009-0000-0619-4094
Z.Y. Wang 0009-0003-2247-0724
M. Nocente 0000-0003-0170-5275
G. Gorini 0000-0002-4673-0901
M. Tardocchi 0000-0001-8443-1809
J. Huang 0000-0001-5662-809X
W. Zhang 0000-0002-5951-6779
X.J. Zhang 0000-0002-8717-354X
G.Q. Zhong 0000-0002-6235-933X
T.S. Fan 0000-0001-9568-174X
B.N. Wan 0000-0002-5483-4807

References

[1] Salewski M. *et al* 2025 Energetic particle physics: chapter 7 of the special issue: on the path to tokamak burning plasma operation *Nucl. Fusion* **65** 043002
[2] Moseev D., Salewski M., Garcia-Muñoz M., Geiger B. and Nocente M. 2018 Recent progress in fast-ion diagnostics for magnetically confined plasmas *Rev. Mod. Plasma Phys.* **2** 7
[3] Stix T.H. 1975 Fast-wave heating of a two-component plasma *Nucl. Fusion* **15** 737
[4] Schneider M. *et al* 2016 Modelling third harmonic ion cyclotron acceleration of deuterium beams for JET fusion product studies experiments *Nucl. Fusion* **56** 112022
[5] Koch R., Van Wassenove G., Van Eester D., Euringer H., Finken K.H., Hillis D.L. and Messiaen A.M. 1995 Interaction of ICRF waves with fast particles on TEXTOR *Plasma Phys. Control. Fusion* **37** A291
[6] Gassner T. *et al* 2012 Deuterium beam acceleration with 3rd harmonic ion cyclotron resonance heating in Joint European Torus: Sawtooth stabilization and Alfvén eigenmodes *Phys. Plasmas* **19** 032115
[7] Sharapov S.E. *et al* 2016 Fusion product studies via fast ion D–D and D–^{3}He fusion on JET *Nucl. Fusion* **56** 112021
[8] Mantsinen M.J., Bobkov V., Gallart D., Geiger B., Johnson T., Meyer H., Nocente M., Ochoukov R., Odstrcil T. and Perelli E. 2016 Third harmonic ICRF heating of deuterium beam ions on ASDEX Upgrade *43rd EPS Conf. on Plasma Physics. European Physical Society* (*Leuven, Belgium*, *4–8 July 2016*)
[9] Zhu G. *et al* 2023 First results from third harmonic ion cyclotron acceleration of deuterium beams in EAST ion heating studies experiments *Nucl. Fusion* **63** 036013
[10] Ericsson G. 2019 Advanced neutron spectroscopy in fusion research *J. Fusion Energy* **38** 330–55
[11] Sangaroon S., Ogawa K. and Isobe M. 2024 Neutron emission spectrometer in magnetic confinement fusion *AAPPS Bull.* **34** 34
[12] Tardocchi M., Nocente M. and Gorini G. 2013 Diagnosis of physical parameters of fast particles in high power fusion plasmas with high resolution neutron and gamma-ray spectroscopy *Plasma Phys. Control. Fusion* **55** 074014
[13] Eriksson J. *et al* 2019 Measuring fast ions in fusion plasmas with neutron diagnostics at JET *Plasma Phys. Control. Fusion* **61** 014027
[14] Hellesen C. *et al* 2013 Fast-ion distributions from third harmonic ICRF heating studied with neutron emission spectroscopy *Nucl. Fusion* **53** 113009
[15] Hellesen C., Mantsinen M., Conroy S., Ericsson G., Eriksson J., Kiptily V.G. and Nabais F. 2018 Analysis of resonant fast ion distributions during combined ICRF and NBI heating with transients using neutron emission spectroscopy *Nucl. Fusion* **58** 056021
[16] Nabais F. *et al* 2022 Bump-on-tail distributions caused by Alfvénic redistribution of energetic ions *Nucl. Fusion* **62** 104001
[17] Eriksson J. *et al* 2015 Dual sightline measurements of MeV range deuterons with neutron and gamma-ray spectroscopy at JET *Nucl. Fusion* **55** 123026
[18] Salewski M. *et al* 2017 MeV-range velocity-space tomography from gamma-ray and neutron emission spectrometry measurements at JET *Nucl. Fusion* **57** 056001
[19] Rud M. *et al* 2025 Velocity-space tomography of MeV-range fast-ion distributions in JET using wave–particle interaction priors *Nucl. Fusion* **65** 112006
[20] Nocente M. *et al* 2020 Generation and observation of fast deuterium ions and fusion-born alpha particles in JET D $-^3$ He plasmas with the 3-ion radio-frequency heating scenario *Nucl. Fusion* **60** 124006

[21] Reman B.C.G. *et al* 2025 Velocity-space tomography of an MeV fast-ion tail generated by three-ion scheme ICRF heating at JET *Nucl. Fusion* **65** 076007
[22] Henriksson H., Conroy S., Ericsson G., Gorini G., Hjalmarsson A., Källne J., Tardocchi M. and Weiszflog M. (JET-EFDA contributors) 2006 Synergetic RF and NB heating effects in JET DT plasmas studied with neutron emission spectroscopy *Nucl. Fusion* **46** 244
[23] Kirov K.K. *et al* 2023 Impact of interaction between RF waves and fast NBI ions on the fusion performance in JET DTE2 campaign *Nucl. Fusion* **64** 016026
[24] Järleblad H. *et al* 2024 Reconstruction of the fast-ion deuterium distribution in a tritium-rich plasma in the JET DTE2 campaign *Nucl. Fusion* **65** 016060
[25] Scholz M. *et al* 2019 Conceptual design of the high resolution neutron spectrometer for ITER *Nucl. Fusion* **59** 065001
[26] Zhang X.J. *et al* 2022 First experimental results with new ICRF antenna in EAST *Nucl. Fusion* **62** 086038
[27] Yang D.K. *et al* 2022 Simulations of neutral beam injection and ion cyclotron resonance heating synergy in high power EAST scenarios *Rev. Sci. Instrum.* **93** 113501
[28] Song C. *et al* 2022 Investigation of the synergistic effects of ICRF+ NBI heating in EAST plasma discharges *Plasma Phys. Control. Fusion* **65** 025003
[29] Zhang W. *et al* 2023 Influence of ICRF-NBI synergy on fast ion distribution and plasma performance in second harmonic heating experiments with deuterium NBI at EAST *Nucl. Fusion* **63** 056015
[30] Zheng Y., Zhang W., Li G., Yin L. and Hao B. 2023 3D simulation of orbit loss and heat load on limiters of ICRF-NBI synergy induced fast ions on EAST *Nucl. Fusion* **63** 046016
[31] Song C. *et al* 2024 Numerical simulations on loss of ICRF-heated NBI ions in EAST *Plasma Phys. Control. Fusion* **66** 075003
[32] Zhong G.Q. *et al* 2016 Status of neutron diagnostics on the experimental advanced superconducting tokamak *Rev. Sci. Instrum.* **87** 11D820
[33] Breslau J., Gorelenkova M., Poli F., Sachdev J., Pankin A., Perumpilly G., Yuan X., and Glant L. 2018 TRANSP 06
[34] Nocente M. 2012 Neutron and gamma-ray emission spectroscopy as fast ion diagnostics in fusion plasmas *Doctoral Thesis* Università degli Studi di Milano-Bicocca
[35] Maslov M. *et al* 2023 JET DT scenario with optimized non-thermal fusion *Nucl. Fusion* **63** 112002
[36] Koning A.J., Rochman D., Sublet J.-C., Dzysiuk N., Fleming M. and Van der Marck S. 2019 TENDL: complete nuclear data library for innovative nuclear science and technology *Nucl. Data Sheets* **155** 1–55
[37] Ge L.J. *et al* 2018 Neutron emission spectroscopy measurements with a compact liquid scintillation detector for NBI-heated plasma at EAST *Plasma Phys. Control. Fusion* **60** 095004
[38] Valentini A., Reman B.C.G., Nocente M., Eriksson J., Järleblad H., Moseev D., Rud M., Schmidt B.S., Snicker A. and Salewski M. 2024 A model for analytical calculations of synthetic neutron energy spectra from beam-target reactions *Nucl. Fusion* **65** 026001
[39] Salewski M. 2019 Fast-ion diagnostic in fusion plasmas by velocity-space tomography
[40] Salewski M. *et al* 2014 On velocity-space sensitivity of fast-ion D-alpha spectroscopy *Plasma Phys. Control. Fusion* **56** 105005
[41] Salewski M. *et al* 2014 Measurement of a 2D fast-ion velocity distribution function by tomographic inversion of fast-ion D-alpha spectra *Nucl. Fusion* **54** 023005
[42] Madsen B. *et al* 2020 Fast-ion velocity-space tomography using slowing-down regularization in EAST plasmas with co-and counter-current neutral beam injection *Plasma Phys. Control. Fusion* **62** 115019
[43] Su J. *et al* 2021 Reconstructions of velocity distributions from fast-ion D-alpha (FIDA) measurements on EAST *Plasma Sci. Technol.* **23** 095103
[44] Salewski M. *et al* 2011 On velocity space interrogation regions of fast-ion collective Thomson scattering at ITER *Nucl. Fusion* **51** 083014
[45] Salewski M. *et al* 2018 Bayesian integrated data analysis of fast-ion measurements by velocity-space tomography *Fusion Sci. Technol.* **74** 23–36
[46] Galdon-Quiroga J. *et al* 2018 Velocity-space sensitivity and tomography of scintillator-based fast-ion loss detectors *Plasma Phys. Control. Fusion* **60** 105005
[47] Schmidt B.S. *et al* 2024 A new FILDSIM model for improved velocity-space sensitivity modelling and reconstructions *Plasma Phys. Control. Fusion* **66** 045004
[48] Schmidt B.S., Salewski M., Reman B., Dendy R.O., Moseev D., Ochoukov R., Fasoli A., Baquero-Ruiz M. and Järleblad H. 2021 Determining 1D fast-ion velocity distribution functions from ion cyclotron emission data using deep neural networks *Rev. Sci. Instrum.* **92** 053528
[49] Schmidt B.S., Salewski M., Reman B.C.G., Dendy R.O., Dong Y., Järleblad H., Moseev D., Ochoukov R., Rud M. and Valentini A. 2023 Velocity-space sensitivity and inversions of synthetic ion cyclotron emission *Phys. Plasmas* **30** 092109
[50] Heidbrink W.W., Garcia A., Boeglin W. and Salewski M. 2021 Phase-space sensitivity (weight functions) of 3 MeV proton diagnostics *Plasma Phys. Control. Fusion* **63** 055008
[51] Jacobsen A.S., Salewski M., Eriksson J., Ericsson G., Bang Korsholm S., Leipold F., Nielsen S.K., Rasmussen J. and Stejner M. (JET EFDA Contributors) 2015 Velocity-space sensitivity of neutron spectrometry measurements *Nucl. Fusion* **55** 053013
[52] Ge L.J. *et al* 2018 Velocity-space sensitivity of time-of-flight neutron spectrometer at EAST in deuterium plasma *Rev. Sci. Instrum.* **89** 10I143
[53] Zhang Y.M. *et al* 2018 Velocity-space sensitivity of the compact neutron emission spectrometers at EAST *Rev. Sci. Instrum.* **89** 10I141
[54] Salewski M. *et al* 2015 Velocity-space observation regions of high-resolution two-step reaction gamma-ray spectroscopy *Nucl. Fusion* **55** 093029
[55] Salewski M. *et al* 2016 Fast-ion energy resolution by one-step reaction gamma-ray spectrometry *Nucl. Fusion* **56** 046009
[56] Järleblad H., Stagner L., Salewski M., Eriksson J., Nocente M., Rasmussen J., Štancar Ž, Kazakov Y.O. and Simmendefeldt B. (JET Contributors) 2022 Fast-ion orbit sensitivity of neutron and gamma-ray diagnostics for one-step fusion reactions *Nucl. Fusion* **62** 112005
[57] Järleblad H. *et al* 2024 Fast-ion orbit origin of neutron emission spectroscopy measurements in the JET DT campaign *Nucl. Fusion* **64** 026015
[58] Pfeiffer W.W., Davidson R.H., Miller R.L. and Waltz R.E. 1980 Onetwo: a computer code for modeling plasa transport in tokamaks *Technical Report* (General Atomics)
[59] Zhang X. *et al* 2014 Diagnosing NB plasmas on the EAST tokamak with new time-of-flight neutron spectrometer *Nucl. Fusion* **54** 104008
[60] Zhang X., Källne J., Gorini G., Nocente M., Fan T., Yuan X., Xie X. and Chen Z. 2014 Second generation fusion neutron time-of-flight spectrometer at optimized rate for fully digital data acquisition *Rev. Sci. Instrum.* **85** 043503
[61] Zhang X. *et al* 2013 A compact stilbene crystal neutron spectrometer for EAST D-D plasma neutron diagnostics *Rev. Sci. Instrum.* **84** 033506

[62] Liao L.Y. *et al* 2021 A compact stilbene crystal neutron spectrometer for NBI-heated plasma neutron diagnostics at EAST *Rev. Sci. Instrum.* **92** 043506
[63] Zhang Y. *et al* 2021 The first experimental results of time-of-flight neutron spectrometer at EAST *J. Fusion Energy* **40** 14
[64] Chen W., Hu L., Zhong G., Hong B., Zhou R., Li K., Huang L. and Cao H. 2021 Design of the radiation shield and collimator for neutron and gamma-ray diagnostics at EAST *Fusion Eng. Des.* **172** 112775
[65] Yuan X. *et al* 2013 Neutron energy spectrum measurements with a compact liquid scintillation detector on EAST *J. Instrum.* **8** 07016
[66] Zhang Y.-Q., Hu L.i.-Q., Zhong G.-Q., Cao H.-R., Zhao J.-L., Yang L.i. and Li. Q. 2023 Development of a high-speed digital pulse signal acquisition and processing system based on MTCA for liquid scintillator neutron detector on EAST *Nucl. Sci. Tech.* **34** 150
[67] Pankin A., McCune D., Andre R., Bateman G. and Kritz A. 2004 The tokamak Monte Carlo fast ion module NUBEAM in the National Transport Code Collaboration library *Comput. Phys. Commun.* **159** 157–84
[68] Brambilla M. 1999 Numerical simulation of ion cyclotron waves in tokamak plasmas *Plasma Phys. Control. Fusion* **41** 1
[69] Kwon J.-M., Chang C.S., Ku S., McCune D. and Phillips C.K. 2006 Development of XGC-RF for global guiding-center particle simulation of minority ICRH heated plasmas in a general tokmak geometry *APS Division of Plasma Physics Meeting Abstracts* vol 48 pp V1–115
[70] Kwon J.-M., McCune D. and Chang C.S. 2007 Enhancement of NUBEAM for the simulation of fast ion and RF-wave interaction based on the quasi-linear theory *APS Division of Plasma Physics Meeting Abstracts* vol 49 pp U8–083
[71] Bertelli N., Gorelenkova M., Podesta M., Valeo E., Green D. and Fredrickson E. 2017 Self-consistent calculation of the effects of RF injection in the HHFW heating regimes on the evolution of fast ions in toroidal plasmas *EPJ Web Conf.* **157** 03004
[72] Sun J. *et al* 2020 Simulations of scattered neutrons for the time-of-flight enhanced diagnostics (TOFED) neutron spectrometer on EAST *Plasma Sci. Technol.* **22** 084004
[73] Cash W. 1979 Parameter estimation in astronomy through application of the likelihood ratio *Astrophys. J.* **228** 939–47
[74] Sahlberg A., Eriksson J., Conroy S., Ericsson G., Hägg L., Giacomelli L. and Belli F. (JET Contributors) 2021 Forward modeling of pile-up events in liquid scintillator detectors for neutron emission spectroscopy *Rev. Sci. Instrum.* **92** 083502
[75] Salewski M. *et al* 2016 High-definition velocity-space tomography of fast-ion dynamics *Nucl. Fusion* **56** 106024
[76] Järleblad H., Stagner L., Salewski M., Eriksson J., Nocente M., Schmidt B.S. and Larsen M.R. 2024 A framework for synthetic diagnostics using energetic-particle orbits in tokamaks *Comput. Phys. Commun.* **294** 108930
[77] Järleblad H. 2024 JuliaFusion/OWCF: a framework for synthetic diagnostics using energetic-particle orbits in tokamaks Version v1.3.0 Apache-2.0 license (available at: https://github.com/JuliaFusion/OWCF) (Accessed 30 September 2024)
[78] Hedin J., Hellsten T., Eriksson L.-G. and Johnson T. 2002 The influence of finite drift orbit width on ICRF heating in toroidal plasmas *Nucl. Fusion* **42** 527
[79] Sun Y.X. *et al* 2025 Fast ion studies in the extended high-performance high βP plasma on EAST *Nucl. Fusion* **65** 016040
[80] Chang J.F., Isobe M., Ogawa K., Huang J., Wu C.R., Xu Z., Jin Z., Lin S.Y. and Hu L.Q. 2016 Scintillator-based fast ion loss measurements in the EAST *Rev. Sci. Instrum.* **87** 11E728
[81] Jin Z., Chang J.F., Huang J., Wu C.R., Xu Z., Chu N., Lin S.Y., Hu L.Q., Isobe M. and Ogawa K. 2017 Extended scintillator-based fast-ion loss diagnostic in the EAST *Fusion Eng. Des.* **125** 160–4
[82] Zhang Y. *et al* 2024 Study on the contribution matrix for EAST radial neutron camera system *Fusion Eng. Des.* **206** 114602
[83] Bigot B. 2019 Progress toward ITER's first plasma *Nucl. Fusion* **59** 112001
[84] BEST 2025 Research Plan: From vision to action: BEST missions and pathways to realisation *Technical Report* (ASIPP & EUROfusion)
[85] Creely A.J. *et al* 2020 Overview of the SPARC tokamak *J. Plasma Phys.* **86** 865860502
[86] Zhang W. *et al* 2022 Conceptual design and optimization of an ITER-type ICRF antenna on CFETR *Nucl. Fusion* **62** 076045
[87] Sundén E.A. *et al* 2013 Evaluation of neutron spectrometer techniques for ITER using synthetic data *Nucl. Instrum. Methods Phys. Res. A* **701** 62–71
[88] Raj P. *et al* 2024 Overview of the neutron diagnostic systems for the SPARC tokamak *Rev. Sci. Instrum.* **95** 103507
[89] Mackie S. *et al* 2024 Ion optical design of the magnetic proton recoil neutron spectrometer for the SPARC tokamak *Rev. Sci. Instrum.* **95** 103502
[90] Rosa M.D. *et al* 2024 Design solutions for the hodoscope of the magnetic proton recoil neutron spectrometer of the SPARC tokamak *Rev. Sci. Instrum.* **95** 083508
[91] Dankowski J. *et al* 2025 Development and performance of the thin-foil proton recoil spectrometer for ITER plasma diagnostics *Fusion Eng. Des.* **219** 115263
[92] Marcinkevicius B. 2024 The thin-foil proton recoil neutron spectrometer for DT plasmas *PhD Thesis* Acta Universitatis Upsaliensis